 doi:10.20944/preprints201705.0168.v1

Article

GNSS-R Ice Sheet Altimetry in Greenland Using TDS-1 Data

Antonio Rius [1,*], Estel Cardellach [1], Fran Fabra [1], Weiqiang Li [1], Serni Ribó [1] and Manuel Hernández-Pajares [2]

[1] Earth Observation Research Group, Institute of Space Sciences (CSIC/IEEC), Barcelona 08193, Spain; cardellach@ice.csic.es (E.C.); fabra@ice.csic.es (F.F.); weiqiang@ice.csic.es (W.L.); ribo@ice.csic.es (S.R.)

[2] UPC-IonSAT, IEEC-CTE-CRAE, Universitat Politècnica de Catalunya, Barcelona 08034, Spain; manuel.hernandez@upc.edu

* Correspondence: rius@ice.csic.es ; Tel.: + 34 93 737 9788

Abstract: Radar altimetry provides valuable measurements to characterize the state and the evolution of the Antartica and Greenland ice sheet cover. Global Navigation Satellite System Reflectometry (GNSS-R) has the potential capacity of complementing the dedicated radar altimeters incrementing the temporal and spatial resolution of the surface height measurements. In this work we perform an study of the Greenland ice sheet using data obtained by the GNSS-R instrument aboard the British TechDemoSat-1 (TDS-1) satellite mission, designed primarily to provide sea state information, like sea surface roughness or wind, but not altimetric products. The data has been analyzed with altimetric methodologies, already proved in aircraft based experiments, to extract signal delay observables to be used to infer the topography of the Greenland cover. The penetration depth of the GNSS signals into ice has also considered. The topographic signal obtained is consistent with those obtained with other passive or active microwave sensors. The main conclusion derived from this work is that GNSS-R also provides valuable measurements of the ice sheet cover and, as taken at a variety of geometries and at least two frequency bands, they prospect different depths into the ice. They have thus potential to complement our understanding of the ice firn and its evolution.

Keywords: GNSS-R; ice sheet; TDS-1; greenland; altimetry

1. Introduction

Greenland and Antarctica hold about 99 percent of the Earth's total freshwater ice. The sea level would rise of the order of several tens of meters if these ice sheets ever melt [1,2]. Even under a partial loss of these enormous ice masses, coastal areas would suffer a significant effect. Recent studies state that mass loss from the Greenland ice sheet currently accounts for ∼10 percent of the observed global mean sea level rise [3], and that some of their glaciers retreat and melt rapidly [4]. There is growing evidence that mass loss from the Antarctic ice sheet is also accelerating [5]. Furthermore, some melting events affect large areas of the ice sheet surfaces within a short time span, such as the extreme event recorded in July 2012, when for one day about 98 percent of Greenland's ice sheet presented signs of surface melting [6]. This possibility requires a precise knowledge of the mass balance of the large ice sheets in Greenland and Antarctica, that is, the difference between the precipitation over the sheets (essentially snowfall) and the effect of different ice loss mechanisms: ablation (evaporation of the ice), surface melt, calving at the interface with the ocean, and melting from contact with the warmer ocean.

One of the techniques to study the ice mass balance uses measurements of the ice elevation taken from satellite altimeters. The changes of the ice topography are evaluated over time to infer the volumetric variation of the ice sheets. The ice sheets topography is also relevant to other scientific questions, such as their influence on weather and climate. For instance, high altitude topographic features of ice caps can alter the storm tracks and they also play a role in the development of dry and cold down-slope winds that reach hurricane forces. These dry cold winds over the ice surface can lead to ablation of the ice, which in turn modifies its topography.

 doi:10.20944/preprints201705.0168.v1

Two distinct types of sensors are used to obtain ice topography from space: dedicated radar and laser altimeters (e.g. NASA's ICESat [7] and ESA's Cryosat-2 [8]) and opportunistic radar altimeters (e.g. ESA's ERS-1, ERS-2, ENVISAT). While the dedicated instruments are optimized to perform altimetry over sea ice and ice sheets, with fine spatial resolution and capability to recover steep slopes of the terrain, the opportunistic ones were not originally intended for ice applications. Nevertheless, their data analysis has contributed to expand the time series of ice topography and mass balance studies back to the times before dedicated missions were launched. The precision of these instruments ranges from decimeters to several meters, and it depends on the employed technique and slope of the terrain [9]. ICESat stopped data acquisition in 2010 and Cryosat-2 is still active but at its final stages, after having doubled its designed lifetime. Current or planned opportunistic altimetric missions include ESA's Sentinel-3 and NASA/CNES Jason-n series, as well as NASA's SWOT. Unfortunately, none of them fully covers the Poles.

In this study we present the preliminary performance of a new opportunistic ice topographic technique. The altimetric retrievals are based on bi-static radar measurements of the delay between the location of a GNSS transmitter of the Global Navigation Satellite System (GNSS), the icy reflecting surface and a low Earth orbiter empowered to capture GNSS signals reflected off the Earth. This technique is called GNSS reflectometry (GNSS-R), and it can be done by demodulating the well-known available codes transmitted by the GNSS satellite (e.g. the Global Positioning System–GPS–C/A codes) or by cross-correlating the reflected radio-link signals against those the line of sight signals. The former approach, named conventional GNSS-R (cGNSS-R), presents coarse delay resolutions as determined by the narrow bandwidth of the public codes. The latter approach, named interferometric GNSS-R (iGNSS-R) makes use of the whole transmitted bandwidth, including the broader bandwidth encrypted codes, of greater delay resolution [10]. Traditionally, cGNSS-R has been linked to ocean scattering applications, such as in the NASA mission CYGNSS [11], which do not require a delay resolution as fine as in altimetric applications. The iGNSS-R was conceived for ocean altimetric purposes with precision assessed to be 2 to 4 times better than those obtained by the conventional cGNSS-R approach [12,13].

2. GNSS-R and the TDS-1 Reflectometry Instrument

Currently, there is no spaceborne experiment to check the actual performance of the iGNSS-R altimetry over ice sheets. The ESA mission GEROS-ISS [16], which plans to include the iGNSS-R technique for ocean altimetry applications, will not cover the main ice sheets because of the low inclination of its orbit. Nevertheless, the UK TDS-1 satellite, a British technological demonstration satellite, carries a payload that takes cGNSS-R measurements during two days out of eight [17]. The TDS-1 satellite was placed into a quasi Sun synchronous orbit with altitude of 635 Km and an inclination of 98.4°, and thus able to cover the whole Greenland sheet and most part of Antarctica. Because of the implementation of the the conventional approach, its altimetric precision is expected to be much coarser than the corresponding to an iGNSS-R instrument. Despite this limitation, in this study we aim to test its performance over the Greenland ice sheet, to be understood as the lowest performance bound of the technique for ice sheet topography. Reference [18] reported altimetry over Greenland using GPS reflected signals found in GPS radio-occultation data collected aboard the German CHAMP satellite. As in UK TDS-1, the observables were also based on conventional GNSS-R, but unlike UK TDS-1 data, they were obtained at very low elevation angles (close to tangential reflection, 0°-1° elevation angles), resulting in purely coherent scattering. In that case, the phase of the electromagnetic field was tracked and used to conduct the altimetry (phase-delay altimetry technique). We could also expect certain degree of coherence in the signals reflected off Greenland ice sheet, as an experiment using cGNSS-R technique over Antarctica ice sheet around Concordia station applied radio-holographic techniques to sense sub-surface snow layers [19]. Nevertheless, the TDS-1 data available over Greenland have been integrated incoherently aboard the satellite, losing the phase information. Therefore, in this study we can only deal with group-delay altimetric techniques.

Preprints (www.preprints.org) | NOT PEER-REVIEWED | Posted: 23 May 2017 doi:10.20944/preprints201705.0168.v1

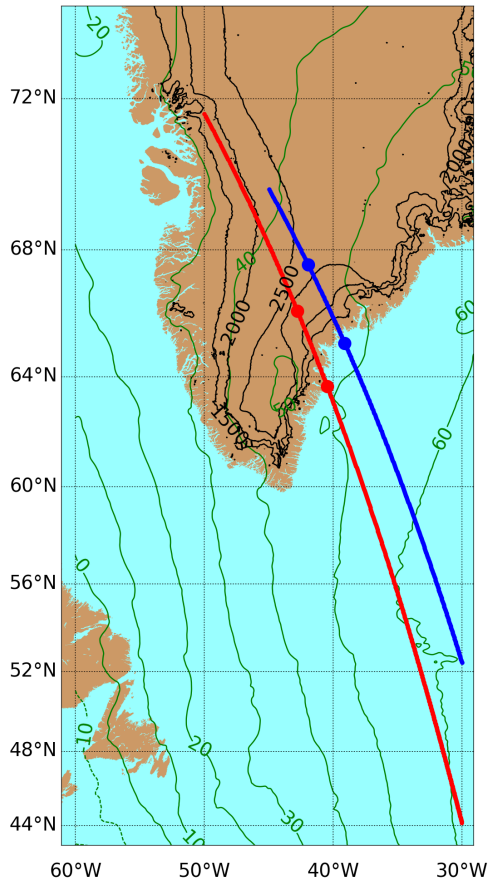

Figure 1. Map of the region considered in this study, containing the southern part of Greenland. The black contour levels over Greenland have been extracted from the National Snow and Ice Data Center (NSIDC) GLAS/ICESat 1 km laser altimetry digital elevation model of Greenland [9]. The green contour lines have been obtained from the Earth Gravitational Model (EGM) 2008 [14]. The two transects correspond to the specular points selected in this study, crossing different Benson facies [15]. The blue trace corresponds to January 26th, 2015, and the red one to the day after. There are two points that divide, from South to North, each trace in three sections, sea, topographic step, and ice, with different prevailing scattering mechanisms. Within these tracks the peak-to-peak variations of the heights with respect WGS84 are on the order of ten meters for the WGM2008 levels, while they are of two kilometers for the (NSIDC) GLAS/ICESat levels.

Data captured by the TDS-1 GNSS-R instrument, hereinafter TDS-1, was made publicly available on March 2015 [20]. The main product is a large set of of Delay Doppler Maps (DDM), defined as the power $P(\tau, f)$ of the correlator output as a function applied delay τ and doppler f offsets respect to a reference. A DDM is provided in a rectangular window of the correlation space (τ, f), with dimensions $(128\ lags, 10,000\ Hz)$. This window is pixeled with cells of dimensions $(1\ lag, 500\ Hz)$.

This data set has been analyzed by different groups to research into the remote sensing possibilities offered by the spaceborne GNSS-R technique. For instance, References [17,20–22] focus on system aspects of TDS-1. The reader is referred to these references for the details of the TDS-1 mission.

Preprints (www.preprints.org) | NOT PEER-REVIEWED | Posted: 23 May 2017 doi:10.20944/preprints201705.0168.v1

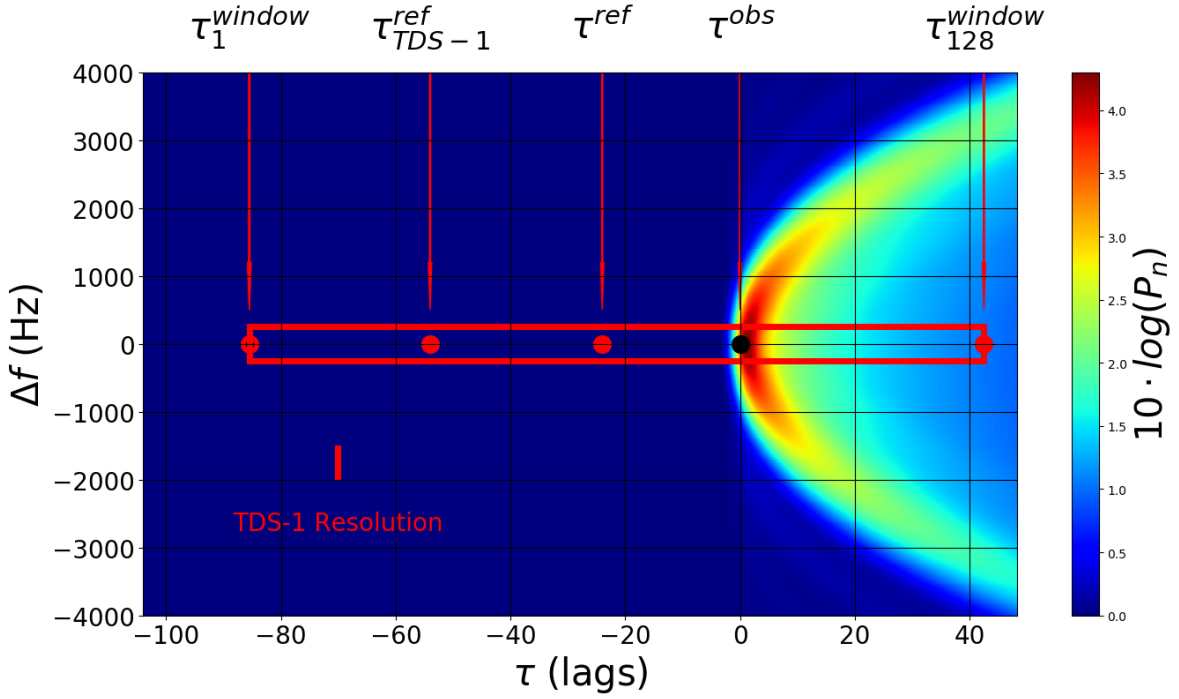

Figure 2. The normalized power $P_n(\tau, \Delta f)$ of a simulated TDS-1 one-second sea DDM, computed with typical values encountered in the TDS-1 situation. The origin of coordinates has been assigned to the point corresponding to the observed delay τ^{obs} and $\Delta f = 0$. The TDS-1 resolution is indicated by the small red box. The larger red rectangle indicates the TDS-1 correlation pixels used in this altimetric study. Beginning and end of the waveform are indicated with the labels τ_1^{window} and τ_{128}^{window}. The point τ_{TDS-1}^{ref} corresponds to the TDS-1 *a priori* reference and τ^{ref} is the corresponding *a priori* value considered in this study.

Sea surface applications are reported in [23] for scatterometry and in [24] for altimetry, while sea ice detection is studied in [25–28]. Soil moisture applications of TDS-1 are given in [29,30] and the ionosphere is studied in [31].

Our study aims to expand the list of applications covering a different objective: the feasibility of near-nadir group-delay altimetric capacity of GNSS-R over ice sheets.

3. Data Set and Models used in this Study

We have analyzed two sets of TDS-1 DDMs gathered on January 26th and 27th, 2015, with specular points over the Ocean and Greenland. In Figure 1 we have represented the specular points corresponding to these sets. In this case we should consider three different scattering mechanisms [32]: surface scattering in the sea surface and ice sheet, volume scattering over the ice and possible multipath when large changes in the slopes of the reflecting surface are present. Consequently, in each track we distinguish three zones, from South to North: sea, topographic step (strong gradient) and ice, depending on the position of the specular point. The points along the step will not be discussed here, because of the difficulties in modeling such reflections.

In Figure 2 we present the main elements needed to establish the relation between the TDS-1 observables and the observables as used in this paper. The size of one cell is indicated in the figure as a small red rectangle. In our study we will only use the Doppler slice corresponding to $f = 0$, shown in the figure as a red long rectangle. The power waveforms represented in Figure 2 are normalized using $P_n = P/P_{noise}$, where P_{noise} is a mean value of the P where there is no signal. The quantity τ^{obs} represents the observable delay assigned to each power waveform, defined as the delay where its

Preprints (www.preprints.org) | NOT PEER-REVIEWED | Posted: 23 May 2017 doi:10.20944/preprints201705.0168.v1

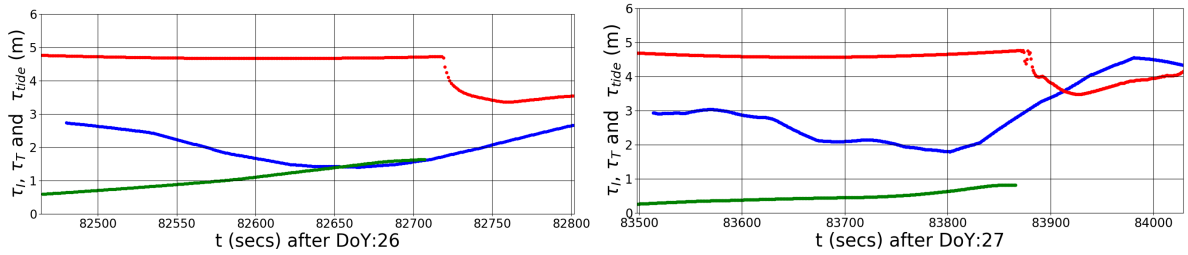

(a) January 26th, 2015.

(b) January 27th, 2015.

Figure 3. The modeled delays, tidal effects τ_{tides} (green), ionospheric τ_{I} (blue) and tropospheric τ_{T} (red), are represented for the two transects.

derivative is maximum [33,34]. The point $\tau^{\mathrm{ref}}_{\mathrm{TDS}-1}$ is the TDS-1 *reference point*. Then the quantity $\delta\tau_{TDS}$ defined as

$$\delta\tau_{\mathrm{TDS}-1} = \tau^{\mathrm{obs}} - \tau^{\mathrm{ref}}_{\mathrm{TDS}-1} \tag{1}$$

contains the observational information to correct the model assumptions used in the definition of $\tau^{\mathrm{ref}}_{\mathrm{TDS}-1}$.

Because the main intended application of the TDS-1 only involves the study of the shape of the power DDMs, the computation of $\tau^{\mathrm{ref}}_{\mathrm{TDS}-1}$ is based on simplified algorithms, and discrepancies on the order of 15 m and 200 Hz are expected, as explained in [20]. In fact, this reference suggest recalculation of this quantity, when better accuracy is needed for other applications.

In this study we use a different reference τ^{ref}. The main differences with respect to $\tau^{\mathrm{ref}}_{\mathrm{TDS}-1}$ are: (a) we consider that the specular points are located either in the EGM2008 [14] or in the NSIDC GLAS/ICESat digital elevation model [9] , and (b) to compute the specular point we consider the position of the transmitter taking into account the signal transit time and its velocity. In our case, the ellipsoidal longitude λ, and latitude ϕ of the specular point corresponds to one reflection on the WGS84 ellipsoid, and the ellipsoidal height h is either an interpolated value of the EGM2008 model, when the specular point is over the sea, or otherwise (NSIDC) GLAS/ICESat. Taking into account these considerations, we define our observed delays $\delta\tau$ as per Equation

$$\delta\tau = \tau^{\mathrm{obs}} - \tau^{\mathrm{ref}} \tag{2}$$

The characteristics of the sea scattering could be interpreted using the Zavorotny-Voronovich model [35], while for the ice case the Ridley surface-volume scattering model could be used [36]. Both models are expressed as the convolution product of two functions, one representing the power waveform of the unscattered signal $\Lambda^2(\tau)$, which is also known as Woodward Ambiguity Function, and the other describing the statistical properties of the scattering media $P_{\mathrm{scatt}}(\tau)$:

$$P(\tau) = \Lambda^2(\tau) * P_{\mathrm{scatt}}(\tau) \tag{3}$$

3.1. Additional Model Components

In addition to the geometrical model considered above to build our observables, we have included other effects whose magnitudes are on the order of a few meters: tidal, tropospheric and ionospheric.

Preprints (www.preprints.org) | NOT PEER-REVIEWED | Posted: 23 May 2017 doi:10.20944/preprints201705.0168.v1

The sea tides delays τ_{tide} for the specular points over the ocean have been modeled by means of the Oregon State University Tidal Inversion Software (OTIS) [37] and using the tidal regional solution for the Atlantic Ocean (2008), with data assimilated from spaceborne altimeters.

The tropospheric delays τ_{T} (in meters) are computed using a first order Saastamonien model and supplemented with a simple mapping function [38]:

$$\tau_{\text{T}} = 2.3 \cdot \frac{P_{\text{atm}}(h)}{P_{\text{atm}}(0)} \frac{2}{\cos(i)} \tag{4}$$

where $P_{\text{atm}}(h)$ is the standard atmospheric pressure at height h, and i is the incidence angle.

The ionospheric delays τ_{I} experienced by the reflected signal have been estimated by means of the Global Ionospheric Maps (GIM) of Vertical Total Electron Content (VTEC) [39], at 5 deg x 2.5 deg x 15 min of resolution in longitude, latitude and time (see this reference for a discussion on the performance of this model in the context of the International GNSS Service (IGS)). In this case the ionospheric delays were moderate, but it should be noted that the ionospheric delays could be one order of magnitude larger in the case of major geomagnetic storms affecting high-latitude regions.

Estimates of these three effects are shown in Figure 3. Other components regularly used in radar altimetry or space geodesy (e.g: ocean and atmospheric loading, surface slope, etc.) have not been considered in this study, given that their corresponding delays, in the sea or ice sections, are much smaller than the uncertainty of our measurements.

3.2. Expected Delay Precision

For the sea case, where the speckle noise is reduced by incoherent averaging of a large quantity of independent power waveforms, reference [10] provides an expression for the estimation of the standard deviation of the delay precision $\sigma_\tau(\tau)$ as

$$\sigma_\tau(\tau^{\text{obs}}) = \frac{S(\tau^{\text{obs}})}{S'(\tau^{\text{obs}})} \frac{1}{\sqrt{N_{\text{inc}}}} \left(1 + \frac{1}{SNR}\right) \tag{5}$$

where $S(\tau^{\text{obs}})$ and $S'(\tau^{\text{obs}})$ are the mean values of the signal part of the waveform and its derivative, SNR is the signal to thermal noise ratio at the observation point, and N_{inc} is the number of independent waveforms taken during the incoherent integration interval.

For the spaceborne scenario, the coherent time of the reflected C/A code signal is expected to be $\sim$1 ms [40] which means that the TDS-1 one-shot power waveforms are essentially uncorrelated.

The first fraction in (5), which can be computed from the measured waveform, or through theoretical simulation, could be taken as 120 m for the spaceborne case. Considering an incoherent average time of 1 sec, i.e. $N_{\text{inc}} = 1000$, and $SNR \approx 0.8$ (SNR values from both data and models agree on this approximate value), the expected uncertainty in the delay measurements precision is $\sim 8.5\ m$.

As mentioned before, and based on the findings in [19], we can expect a slightly more coherent reflection process over the smooth ice sheets. Nevertheless, it is also likely that it has a significant component of volumetric scattering, reshaping the waveform and redistributing its energy along the delay axis. Overall, the data show that SNR levels both sea and ice sheets are of the same order of magnitude and as a consequence we can expect similar levels of uncertainty.

3.3. Selected Waveforms over Greenland

As stated before, we have selected two sets of TDS-1 waveforms obtained over Greenland. The selection criteria have been: (a) tracks obtained in two consecutive days -26 and 27 January 2015-, (b) tracks transmitted by the same GPS satellite -PRN 31-, (c) tracks with relatively small incidence angles and (d) high antenna gain toward the nominal specular position. These criteria have been chosen to obtain quality data to facilitate comparisons.

Preprints (www.preprints.org) | NOT PEER-REVIEWED | Posted: 23 May 2017 doi:10.20944/preprints201705.0168.v1

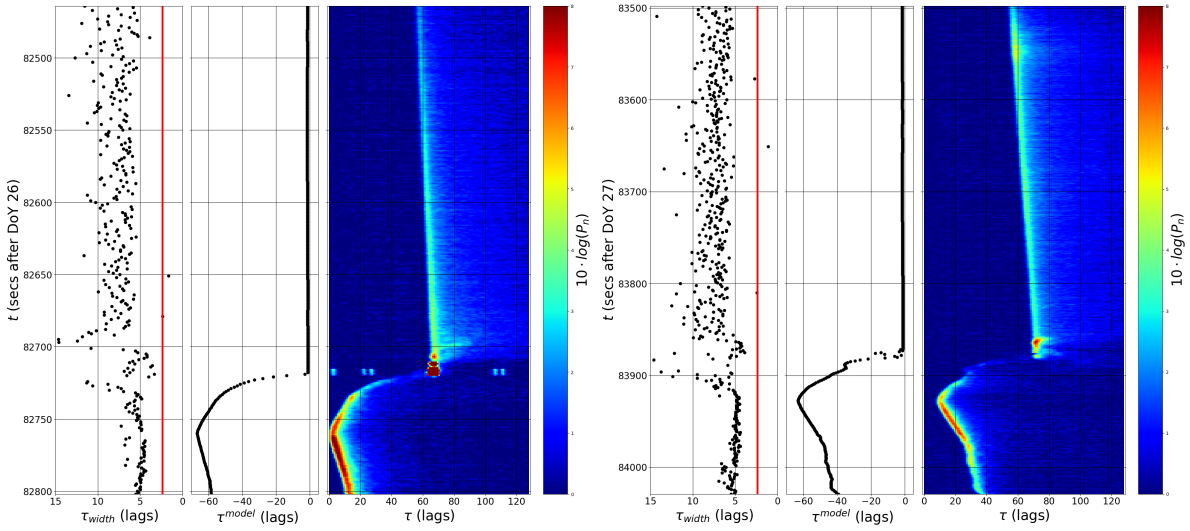

(a) January 26th, 2015 **(b)** January 27th, 2015

Figure 4. Two panels showing the time evolution of the power waveforms, for each track. The graph to the left of each respective panel contain the waveform widths τ_{width}, defined at their 3-dB level. The vertical red line corresponds to the width of unscattered GPS C/A code signals. In the middle figure of each panel we show the modeled delay τ^{model} as expected with respect to a reflection off a point on the reference WGS-84 ellipsoid. The model has assumed surface topographies provided by the EGM 2008 geoid over the sea and by NSIDC GLAS/ICESat over Greenland. In the right figure of each panel we present all the waveforms 2D image.

Table 1 summarizes the relevant parameters defining both data transects.

Table 1. Selected TDS Data

Variable	First Transect	Second Transect
Second of Day UTC	82470-82800 (s)	83500-84200 (s)
Incidence angle i	3-19 (°)	4-28 (°)
Gain	8-12 (dBi)	8-13 (dBi)

In Figure 4 we have represented the normalized power waveforms P_{n}, in dB, as a function of the second of the day t and the correlator lag τ for both days. To facilitate the interpretation of the power waveforms, we include in the central panel the modeled delay τ^{model}, here understood as the delay with respect to an hypothetical reflection off the reference ellipsoid WGS84. These modeled delays are derived assuming that the sea surface elevation corresponds to the EGM 2008 and the ice surface elevation corresponds to the topography given by NSIDC GLAS/ICESat. It should be noticed (a) the nearly linear variation of the peak delay of the sea waveforms -probably related to the open loop nature of the TDS-1 tracking, uncertainties in the determination of the transmitter trajectory or other instrumental causes, (b) the high correlation between the variable τ^{model} and the peak delays of the ice waveforms and (c) the reduced number of waveforms visible in the topographic step region, due to the limitations of the model used to track the reference point.

As it has been indicated in Equation (3), the power waveforms could be expressed as the convolution product $P(\tau) = \Lambda^2(\tau) * P_{\text{scatt}}(\tau)$. In the reference [41, p. 143], it is shown that the variance of this $P(\tau)$ should be the sum of the variances of the two factors $\Lambda^2(\tau)$ and $P_s(\tau)$. Because in our case $\Lambda^2(\tau)$ is fixed, the variance of the power waveform will be a measure of the of the scattering. As indicator of such variance, we use the 3 dB widths τ_{width} of the power waveforms. In Figure 4 we

Preprints (www.preprints.org) | NOT PEER-REVIEWED | Posted: 23 May 2017 doi:10.20944/preprints201705.0168.v1

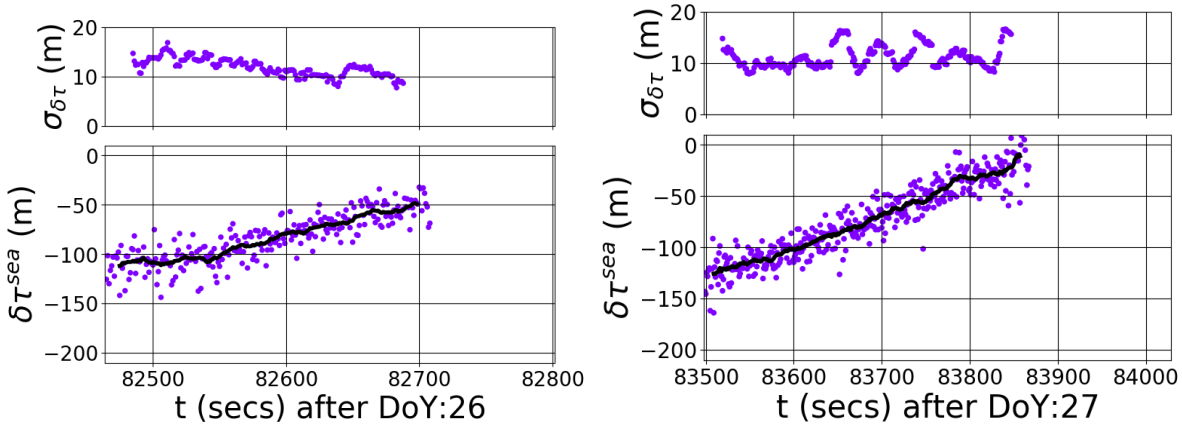

(a) January 26th, 2015.

(b) January 27th, 2015.

Figure 5. The observed delays $\delta\tau^{\text{sea}}$ and its standard deviation $\sigma_{\delta\tau}$ obtained from the *sea* waveforms and their standard deviation. Superimposed to the values $\delta\tau^{\text{sea}}$ we include a running mean used to derive $\sigma_{\delta\tau}$. The trend in the observed delays is attributed in this study to clock inaccuracies effects

have included a third panel with these quantities. These quantities are a source of information of the reflecting media. It is shown a systematic difference between sea and ice waveform widths that will produce different bias in the determination of the delay [34].

4. Results

In Figure 5 we have represented the observed delays $\delta\tau^{\text{sea}}$ and their standard deviation over the sea section. These data over the sea have been used to estimate the nearly linear variation of the observed sea delays, unexplained by any geophysical phenomena. We consider these variations as observational nuisance effects to be calibrated. We have extrapolated this variations to all the observation interval, and we have removed this variation to all observations (including those over the ice sheets). The corresponding calibrated observations are presented in Figure 6. From these quantities we derive the *apparent* height variation δh computed as

$$\delta h^{\text{apparent}} = -\frac{1}{2}\cos(i)\cdot\delta\tau \tag{6}$$

which are represented in Figures 7. The use of the superscript *apparent* is introduced here to express that this interpretation would assume that the extra delay $\delta\tau$ is either due to a shift of the reflecting surface below our reference or that it is due to the reflection coming from inside the ice, for wich the refractive index of the ice is not properly accounted.

If we instead assume that our topographic reference is correct and that the extra delay $\delta\tau$ is due to signal being scattered from inside the ice sheet, then we need to account for the actual refractive index of the ice. In this case, the vertical distance from which such reflection would occur will be referred as *physical* instead of *apparent*. An approximate relation between *apparent* heights and its *physical* counterpart could be obtained assuming that (a) the complex dielectric constant ϵ_{ice} is uniform within the the ice sheet, (b) its imaginary component is negligible, and (c) its refractive index is $n_{\text{ice}} = \sqrt{\epsilon_{\text{ice}}}$. A signal entering to the ice sheet, from the air ($n_{\text{air}} = 1$) with an incidence angle $i = i_{\text{air}}$ will be refracted into the direction i_{ice} defined by the Snell's Law as

$$\sin(i_{\text{ice}}) = \frac{n_{\text{air}}}{n_{\text{ice}}}\sin(i_{\text{air}}) \tag{7}$$

Preprints (www.preprints.org) | NOT PEER-REVIEWED | Posted: 23 May 2017 doi:10.20944/preprints201705.0168.v1

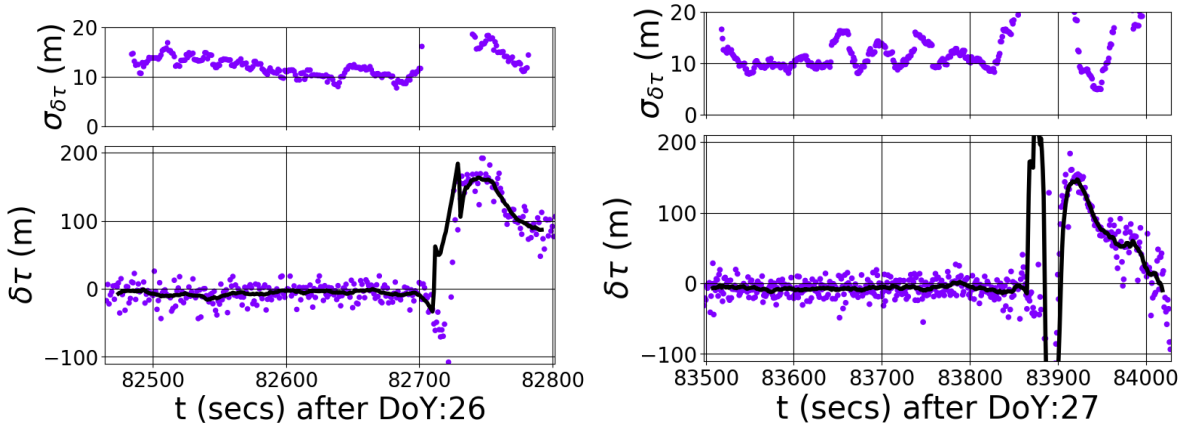

(a) January 26th, 2015. **(b)** January 27th, 2015.

Figure 6. The differential delays $\delta\tau$ and its standard deviation $\sigma_{\delta\tau}$ obtained with the whole data set, after correcting the trend derived from the sea waveforms. Superimposed to the values $\delta\tau^{\text{sea}}$ we include a running mean used to derive $\sigma_{\delta\tau}$

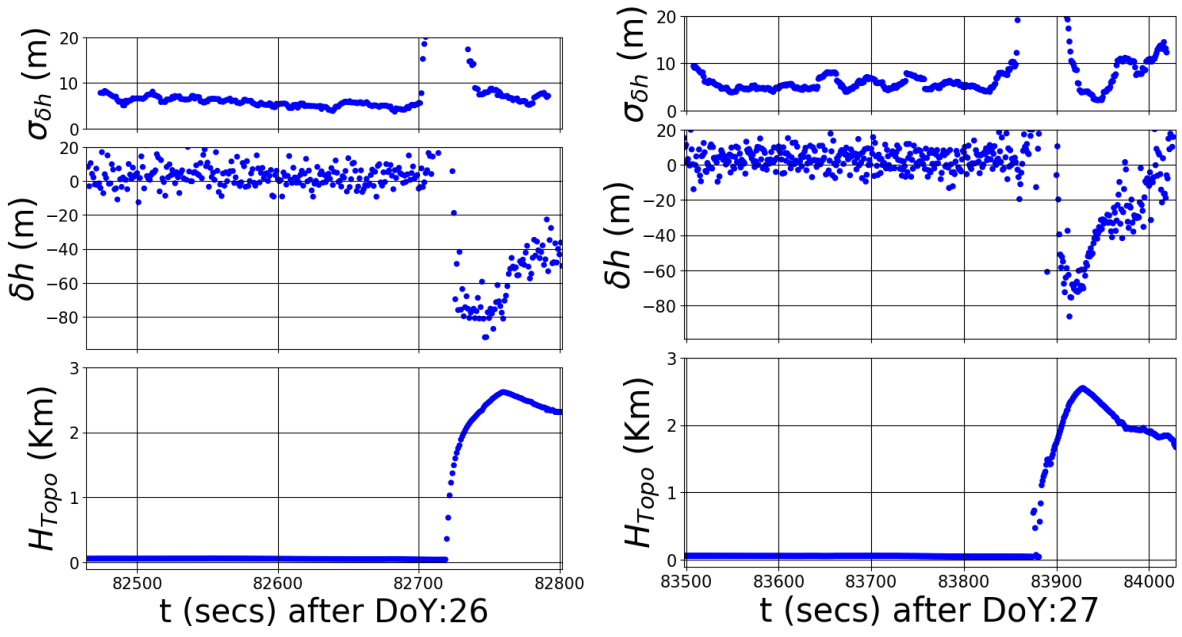

(a) January 26th, 2015. **(b)** January 27th, 2015.

Figure 7. In each column we have represented from bottom to top 1) the topography associated to each track H_{Topo}, 2) the estimate of the *apparent* the height relative to the *a priori* model $\delta h^{\text{apparent}}$, and 3) its standard deviation $\sigma_{\delta h}$.

Preprints (www.preprints.org) | NOT PEER-REVIEWED | Posted: 23 May 2017 doi:10.20944/preprints201705.0168.v1

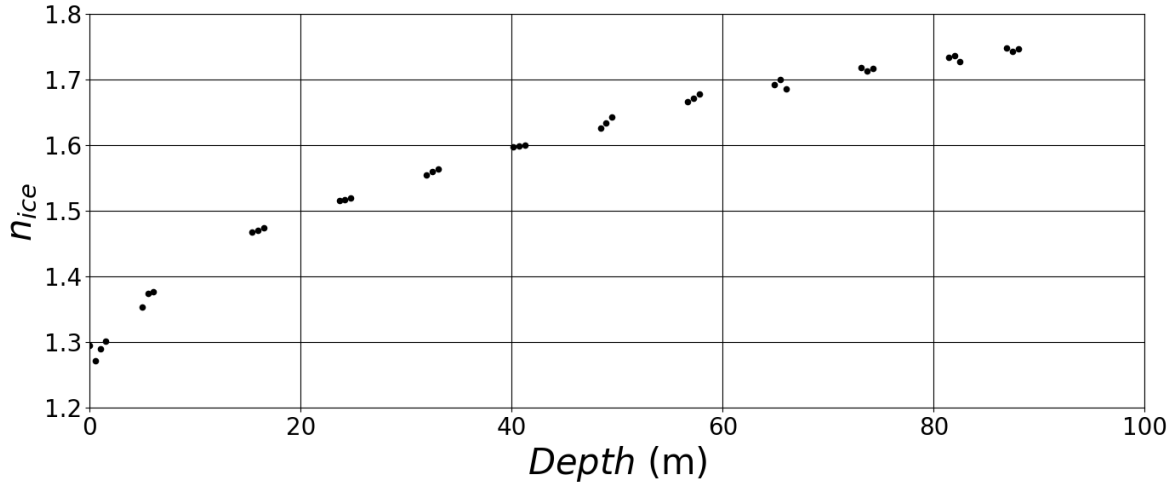

Figure 8. Refractive index as a function of ice depth, as reported in Table 4 of Ref [42], estimated from North Greenland Eemian Ice Drilling (NEEM) camp data.

Consequently, for a signal entering with an incidence angle i, the relation between the *physical* height δh^{phys} and its *apparent* counterpart $\delta h^{\text{apparent}}$ could be written as:

$$\delta h^{\text{phys}} = F(n_{\text{ice}}, i_{\text{air}}) \cdot \delta h^{\text{apparent}} \tag{8}$$

where the mapping F is defined as:

$$F(n_{\text{ice}}, i_{\text{air}}) = \frac{n_{\text{air}}}{n_{\text{ice}}} \frac{\cos(i_{\text{ice}})}{\cos(i_{\text{air}})} \tag{9}$$

Reference [43, p. 848] explains that the refractive index within the ice sheet is a function of its depth, being a weighted mean of air ($n_{\text{air}} = 1$) and pure ice ($n_{pure\ ice} = \sqrt{3.15}$, in the microwave region) refractive indices. To have an order of magnitude value of the expected refractive index in the Greenland ice sheet, we show in Figure 8 a profile of n_{ice}, based on Table 4 of Reference [42, Table 4]. This was obtained as a result of the analysis of data obtained from one of the firn cores drilled down to 88.55 m in the North Greenland Eemian Ice Drilling (NEEM) camp, northwest Greenland at an elevation of 2450 m.

A recent analysis of data taken by the radar Tandem-X (TDX) mission [44], provides information on the ice refractive index in Greenland showing variations in the range [1.3-1.4] and an average penetration depths on the order of 4 meters for the dry-snow facie. This range of values for the refractive index is consistent with the values near the surface (TDX penetration) in Figure 8. The TDX radar operates at 9.6 GHz, approximately six times higher than the GNSS-R L1 frequency (1.6 GHz), and, as a first approximation, assuming that the properties of the ice sheet are constant, we could consider that at the GPS frequency the penetration depth is on the order of 24 meters. Then, from Figure 8 we take $n_{\text{ice}} = 1.5$ as a representative value for our L-band case. Taking into account the limited range of incidence angles of our observations (see Table 1) and the uncertainties associated to our choice of n_{ice} we have approximated Equation (9), with the constant $F = 0.70$. The corresponding *physical* heights computed using Equation (8) are indicated in the left panel of Figure 9. Note that the interpretation of negative *physical* heights corresponds to the depths inside the ice from where the reflected signal comes. In fact, L-band signals can penetrate into the dry snow deeper than 24 meter, as reported in the GNSS-R ground-based experiment conducted at Concordia Station in Antarctica [19]. Therefore, the obtained *physical* depths are within the findings in Concordia Station campaign.

Preprints (www.preprints.org) | NOT PEER-REVIEWED | Posted: 23 May 2017 doi:10.20944/preprints201705.0168.v1

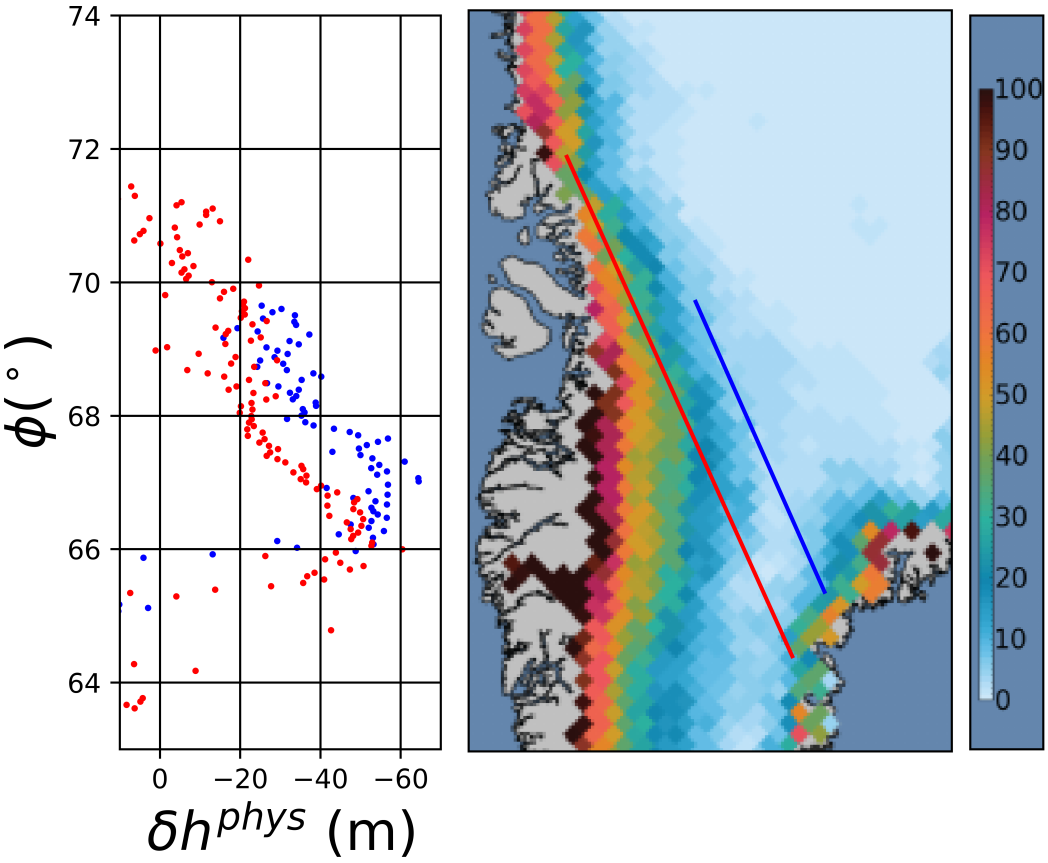

Figure 9. Left) Estimates of δh^{phys} as a function of the latitude of the specular point for the January 26th, 2015 track (blue), and the January 27th, 2015 (red). Right) Section of the Greenland Map, courtesy of University of Georgia/Thomas Mote, supplied by the National Snow and Ice Data Center, University of Colorado, showing the number of melting days [45], indicated by the color scale, for the period January-October 2016. The two traces correspond to the approximate location of the specular points considered.

Moreover, this implies that higher values of n_{ice} could also be justified, which would reduce the factor $F(n_{\text{ice}}, i_{\text{air}})$ (thus also reducing δh^{phys}, i.e. bringing it closer to the external air-ice interface).

4.1. Comparisons

Some comparisons between our results, and those obtained with other techniques used to characterize the Greenland ice sheet are possible. As expected, such comparisons will show biases induced by the resolution of the TDS-1, by our choice of the refractive index and by the fact that the results to be compared have been obtained at frequencies with different penetration depth, and the extraction of the observed delays τ^{obs} will have different delays for the sea and ice sections.

First we compare our δh^{phys} results with the melting extent of the Greenland ice sheet, measured with passive microwave instruments [45]. This is done in Figure 9, where it is shown δh^{phys} in parallel with a map of the NSIDC Greenland Cumulative Melt Days (GCM). The ice depth retrieved might be a potential measurement of the homogeneity of the internal ice structure, thus related to the number of melting events through the season.

A second assessment could be obtained by comparing our results with those obtained with radar altimetry missions in Greenland. Reference [44] compares ICESat laser altimetric measurements h_{ICESat}, which essentially sense the external air-snow interface, and the X-band microwave DEM measured

 doi:10.20944/preprints201705.0168.v1

with Tandem-X (TDX), h_{TDX}. The differences $\Delta h_{\mathrm{TDX}} = h_{\mathrm{ICESat}} - h_{\mathrm{TDX}}$, for different facies, are in the range $[3.54 - 6.82]$ meters with standard deviations in the order of two meters. The extrapolation from X-band to L-band, for the upper limit of this range, and taking into account the uncertainties of their measurements, i.e. 8.82 meter, would bring the L-band depth around ∼-53 meters, which is higher (less deep) than the deepest value obtained with TDS-1, of δh^{phys} ∼-60 meters, shown in Figure 9. If n_{ice} had been assumed as 1.7, roughly corresponding to 60 meter depth (see Figure 8), then the F factor would have resulted in a lower number (∼0.62), which would have produced a deepest physical depth of δh^{phys} ∼-49 meter, which is closer to the X-to-L band extrapolation of the Tandem-X results. Therefore, considering the simplicity of the model used here, which does not account for the internal variations of the ice refractive index, and the associated uncertainty in the single n_{ice} value used in Equation (9), the results obtained present the same order of magnitude as the X-to-L band extrapolation exercise.

The comparison is also affected by the dispersion of the data (of the order of 10 meter in 1 second sampling), and probably biased by residual effects. One of the residual effects is related with the instrumentation used: the TDS-1 GNSS-R receiver has very low delay resolution (75 meter, larger than δh^{phys}), and this coarse sampling may introduce biases which in turn can be different over the sea (broader shaped waveforms) from those biases over the ice (narrower shaped waveforms, see the differences in τ_{width} in Figure 4). Therefore, the calibration strategy presented in Section 4, with corrections estimated from the tracks segments over the sea, might not fully correct the potential biases over ice. Future instrumentation capturing signals with correlators with higher resolution and wider signals, such as the payload planned for GEROS-ISS mission [16], should help in reducing this problem.

5. Discussion and Conclusions

As shown in the sections above, the GNSS signals reflected off the Greenland ice sheet appear to be scattering from within the ice, that is, from a given penetration depth. This depth depends on several factors, some of them well known, as the geometry of the observation and the electromagnetic carrier frequency of the signals, and some others not fully characterized, such as the air-ice interface and the internal structure of ice densities.

The surface elevation of the Greenland ice sheet has slow variations in time, in the order of a few cm/yr in the driest high areas and up to 50 cm/yr in the lower percolation and ablation zones [46]. GNSS-R missions have potential to cover zones of the size of Greenland in periods of time much shorter than one year [e.g. 16]. During these periods, therefore, a relatively large number of GNSS-R measurements over a certain area of Greenland would be acquired for which the surface elevation could be considered stationary. The accumulated information in such a set of measurements, taken at different geometries and even at different carrier frequencies (the GNSS systems transmit at three different frequencies simultaneously) could be combined to contribute in characterizing different depths of the sheet, potentially mapping the variations in δh^{phys} into variation of the ice conditions at these different depths. For example, the American GNSS system, the Global Positioning System (GPS) transmit at L1 (1.575 GHz received by TDS-1 reflectometry receiver) as well at L2 (1.228 GHz) and L5 (1.176 GHz), which according to the frequency band extrapolation exercise would have resulted in physical depths 28% and 34% deeper than δh^{phys} here found for L1. Combination with measurements taken with other technologies (SAR, radar altimeters, laser altimeters) working at different bands of the electromagnetic spectrum would further complement the GNSS-R data, especially for depths closer to the surface as they often operate at carrier frequencies higher than L-band.

The question then is whether the precision of such measurements would be sufficiently fine to capture the expected variations in the ice firn. One one hand, a series of sudden changes should easily be detectable, with signatures much larger than the dispersion of the measurements: for example the melting of the external surface layer, the formation of a temporary supraglacial pond, or the appearance of new sub-surface draining flows. As liquid water has much larger permittivity than ice

Preprints (www.preprints.org) | NOT PEER-REVIEWED | Posted: 23 May 2017 doi:10.20944/preprints201705.0168.v1

and nearly no penetration depth, such events should dramatically change δh^{phys} to match the vertical location of the liquid water. Subglacial drainage systems are not known precisely, and they represent a relevant component of the ice sheet hydrology, which in turn affects the ice sheet balance and it has implications for future sea level rise [e.g. 47]. On the other hand, seasonal variations in the ice sheet might also occur, and [42, Figure 1] indicates ∼3.5% variations in the refractive index between the deposition season (summer to autumn) and the rest of the year in most ice depths down to 80 meter. These variations induce variations in F and δh^{phys} of the same order as those in n_{ice}, which at the deepest zones found in our study correspond to variations of ∼3 meter, and ∼1.5 meter in intermediate altitude zones. These variations are smaller than the 1 second standard deviation found in the height measurements of this TDS-1 set (∼10 meter), but perfectly achievable when combining measurements over the same area within the sub-year time period of interest ($(\sigma_h/3)^2$ ∼11 measurements needed to achieve 3 meter precision and $(\sigma_h/1.5)^2$ ∼44 measurements to reach 1.5 meter).

Finally, we are reminded that other studies with GNSS-R signals reflected off ice sheets have shown coherence of the reflected signals, and carrier phase information has been used for altimetric and sub-surface sensing [18,19], but that in these particular events TDS-1 did not acquire them, but only incoherently integrated observables. This limitation, nevertheless, could be re-examined as TDS-1 is capable of acquiring unprocessed raw data for short periods of time, and thus could also be tested off ice sheets in Greenland or Antarctica. Unfortunately, other TDS-1 limitations are not as simple to overcome and in some cases a different sort of GNSS-R payload would be required to fully test the capabilities of this technique, with signals of broader bandwidth and much higher sampling rates [16, e.g.].

Acknowledgments: This work has been carried out with the financial support of the Spanish research project ESP2015-70014-C2-2-R (MINECO/FEDER).

Author Contributions: A.R coordinated the study. A.R, E.C, F.F., W.L. and S.R contributed equally to the analysis and interpretation of the GNSS-R aspects of this study. M.H-P contributed to the analysis and interpretation of the ionospheric part.

Conflicts of Interest: The authors declare no conflict of interest. The funding sponsors had no role in the design of the study, in the collection, analyses, or interpretation of data, in the writing of the manuscript, and in the decision to publish the results.

Abbreviations

The following abbreviations are used in this manuscript:

CYGNSS	Cyclone Global Navigation Satellite System
DDM	Delay-Doppler Map
DEM	Digital Elevation Model
EGM	Earth Gravitational Model
GCM	Greenland Cumulative Melt
GIM	Global Ionospheric Maps
GNSS	Global Navigation Satellite System
GNSS-R	GNSS Reflectometry
cGNSS-R	Conventional GNSS-R
iGNSS-R	Interferometric GNSS-R
GPS	Global Positioning System
IGS	International GNSS Service
NEEM	North Greenland Eemian Ice Drilling
NSIDC	National Snow and Ice Data Center
SNR	Signal-to-Noise Ratio
TDS	TechDemoSat
TDX	Tandem-X Mission
VTEC	Vertical Total Electron Content
WGS	World Geodetic System

 doi:10.20944/preprints201705.0168.v1

References

1. Gregory, J.M.; Huybrechts, P.; Raper, S.C.B. Climatology: Threatened loss of the Greenland ice-sheet. *Nature* **2004**, *428*, 616–616.
2. Lythe, M.B.; Vaughan, D.G. BEDMAP: A new ice thickness and subglacial topographic model of Antarctica. *Journal of Geophysical Research: Solid Earth* **2001**, *106*, 11335–11351.
3. Church, J.A.; Clark, P.U.; Cazenave, A.; Gregory, J.M.; Jevrejeva, S.; Leverman, A.; Merrifield, M.A.; Milne, G.A.; Nerem, R.S.; Nunn, P.D.; Payne, A.J.; Pfeffer, W.T.; Stammer, D.; Unnikrishnan, A.S. Sea Level Change. In *Climate Change 2013: The Physical Science Basis. Contribution of Working Group I to the Fifth Assessment Report of the Intergovernmental Panel on Climate Change*; Cambridge University Press: United Kingdom and New York, NY, USA, 2013.
4. Mouginot, J.; Rignot, E.; Scheuchl, B.; Fenty, I.; Khazendar, A.; Morlighem, M.; Buzzi, A.; Paden, J. Fast retreat of Zachariæ Isstrøm, northeast Greenland. *Science* **2015**, *350*, 1357–1361.
5. McMillan, M.; Shepherd, A.; Sundal, A.; Briggs, K.; Muir, A.; Ridout, A.; Hogg, A.; Wingham, D. Increased ice losses from Antarctica detected by CryoSat-2. *Geophysical Research Letters* **2014**, *41*, 2014GL060111.
6. Nghiem, S.V.; Hall, D.K.; Mote, T.L.; Tedesco, M.; Albert, M.R.; Keegan, K.; Shuman, C.A.; DiGirolamo, N.E.; Neumann, G. The extreme melt across the Greenland ice sheet in 2012. *Geophysical Research Letters* **2012**, *39*, L20502.
7. Zwally, H.J.; Schutz, B.; Abdalati, W.; Abshire, J.; Bentley, C.; Brenner, A.; Bufton, J.; Dezio, J.; Hancock, D.; Harding, D.; Herring, T.; Minster, B.; Quinn, K.; Palm, S.; Spinhirne, J.; Thomas, R. ICESat's laser measurements of polar ice, atmosphere, ocean, and land. *Journal of Geodynamics* **2002**, *34*, 405–445.
8. Wingham, D.J.; Francis, C.R.; Baker, S.; Bouzinac, C.; Brockley, D.; Cullen, R.; de Chateau-Thierry, P.; Laxon, S.W.; Mallow, U.; Mavrocordatos, C.; Phalippou, L.; Ratier, G.; Rey, L.; Rostan, F.; Viau, P.; Wallis, D.W. CryoSat: A mission to determine the fluctuations in Earth's land and marine ice fields. *Advances in Space Research* **2006**, *37*, 841–871.
9. Brenner, A.C.; DiMarzio, J.P.; Zwally, H.J. Precision and Accuracy of Satellite Radar and Laser Altimeter Data Over the Continental Ice Sheets. *IEEE Transactions on Geoscience and Remote Sensing* **2007**, *45*, 321–331.
10. Martin-Neira, M.; D'Addio, S.; Buck, C.; Floury, N.; Prieto-Cerdeira, R. The PARIS Ocean Altimeter In-Orbit Demonstrator. *IEEE Transactions on Geoscience and Remote Sensing* **2011**, *49*, 2209–2237.
11. Ruf, C.; Unwin, M.; Dickinson, J.; Rose, R.; Rose, D.; Vincent, M.; Lyons, A. CYGNSS: Enabling the Future of Hurricane Prediction [Remote Sensing Satellites]. *IEEE Geoscience and Remote Sensing Magazine* **2013**, *1*, 52–67.
12. Cardellach, E.; Rius, A.; Martin-Neira, M.; Fabra, F.; Nogués-Correig, O.; Ribó, S.; Kainulainen, J.; Camps, A.; D'Addio, S. Consolidating the Precision of Interferometric GNSS-R Ocean Altimetry Using Airborne Experimental Data. *IEEE Transactions on Geoscience and Remote Sensing* **2014**, *52*, 4992–5004.
13. Camps, A.; Park, H.; Domènech, E.V.i.; Pascual, D.; Martin, F.; Rius, A.; Ribó, S.; Benito, J.; Andrés-Beivide, A.; Saameno, P.; Staton, G.; Martín-Neira, M.; D'Addio, S.; Willemsen, P. Optimization and Performance Analysis of Interferometric GNSS-R Altimeters: Application to the PARIS IoD Mission. *IEEE Journal of Selected Topics in Applied Earth Observations and Remote Sensing* **2014**, *7*, 1436–1451.
14. Pavlis, N.K.; Holmes, S.A.; Kenyon, S.C.; Factor, J.K. The development and evaluation of the Earth Gravitational Model 2008 (EGM2008). *Journal of Geophysical Research: Solid Earth* **2012**, *117*, B04406.
15. Benson, C. Stratigraphic studies in the snow and firn of the Greenland ice sheet. Technical report, Cold Regions Research And Engineering Lab Hanover N H, 1962.
16. Wickert, J.; Cardellach, E.; Martín-Neira, M.; Bandeiras, J.; Bertino, L.; Andersen, O.B.; Camps, A.; Catarino, N.; Chapron, B.; Fabra, F.; Floury, N.; Foti, G.; Gommenginger, C.; Hatton, J.; Høeg, P.; Jäggi, A.; Kern, M.; Lee, T.; Li, Z.; Park, H.; Pierdicca, N.; Ressler, G.; Rius, A.; Roselló, J.; Saynisch, J.; Soulat, F.; Shum, C.K.; Semmling, M.; Sousa, A.; Xie, J.; Zuffada, C. GEROS-ISS: GNSS REflectometry, Radio Occultation, and Scatterometry Onboard the International Space Station. *IEEE Journal of Selected Topics in Applied Earth Observations and Remote Sensing* **2016**, *9*, 4552–4581.
17. Unwin, M.; Jales, P.; Tye, J.; Gommenginger, C.; Foti, G.; Rosello, J. Spaceborne GNSS-Reflectometry on TechDemoSat-1: Early Mission Operations and Exploitation. *IEEE Journal of Selected Topics in Applied Earth Observations and Remote Sensing* **2016**, *9*, 4525–4539.

18. Cardellach, E.; Ao, C.O.; de la Torre Juárez, M.; Hajj, G.A. Carrier phase delay altimetry with GPS-reflection/occultation interferometry from low Earth orbiters. *Geophysical Research Letters* **2004**, *31*, L10402.
19. Cardellach, E.; Fabra, F.; Rius, A.; Pettinato, S.; D'Addio, S. Characterization of dry-snow sub-structure using GNSS reflected signals. *Remote Sensing of Environment* **2012**, *124*, 122–134.
20. Jales, P.; Unwin, M. MERRByS product manual: GNSS-Reflectometry on TDS-1 with the SGR-ReSI. *Surrey Satellite Technol. Ld. Guildford, UK* **2015**.
21. Jales, P. Spaceborne receiver design for scatterometric GNSS reflectometr. PhD thesis, University of Surrey, United Kingdom, 2012.
22. Schiavulli, D.; Nunziata, F.; Migliaccio, M.; Frappart, F.; Ramilien, G.; Darrozes, J. Reconstruction of the Radar Image From Actual DDMs Collected by TechDemoSat-1 GNSS-R Mission. *IEEE Journal of Selected Topics in Applied Earth Observations and Remote Sensing* **2016**, *9*, 4700–4708.
23. Foti, G.; Gommenginger, C.; Jales, P.; Unwin, M.; Shaw, A.; Robertson, C.; Roselló, J. Spaceborne GNSS reflectometry for ocean winds: First results from the UK TechDemoSat-1 mission. *Geophysical Research Letters* **2015**, *42*, 2015GL064204.
24. Clarizia, M.P.; Ruf, C.; Cipollini, P.; Zuffada, C. First spaceborne observation of sea surface height using GPS-Reflectometry. *Geophysical Research Letters* **2016**, *43*, 2015GL066624.
25. Yan, Q.; Huang, W. Spaceborne GNSS-R Sea Ice Detection Using Delay-Doppler Maps: First Results From the U.K. TechDemoSat-1 Mission. *IEEE Journal of Selected Topics in Applied Earth Observations and Remote Sensing* **2016**, *9*, 4795–4801.
26. AlonsoArroyo, A.; Zavorotny, V.U.; Camps, A. Sea ice detection using GNSS-R data from UK TDS-1. 2016 IEEE International Geoscience and Remote Sensing Symposium (IGARSS), 2016, pp. 2001–2004.
27. Hu, C.; Benson, C.; Rizos, C.; Qiao, L. Single-Pass Sub-Meter Space-Based GNSS-R Ice Altimetry: Results From TDS-1. *IEEE Journal of Selected Topics in Applied Earth Observations and Remote Sensing* **2017**, *PP*, 1–7.
28. Yan, Q.; Huang, W.; Moloney, C. Neural Networks Based Sea Ice Detection and Concentration Retrieval From GNSS-R Delay-Doppler Maps. *IEEE Journal of Selected Topics in Applied Earth Observations and Remote Sensing* **2017**, *PP*, 1–10.
29. Camps, A.; Park, H.; Pablos, M.; Foti, G.; Gommenginger, C.; Liu, P.W.; Judge, J. Soil moisture and vegetation impact in GNSS-R TechDemosat-1 observations. 2016 IEEE International Geoscience and Remote Sensing Symposium (IGARSS), 2016, pp. 1982–1984.
30. Chew, C.; Shah, R.; Zuffada, C.; Hajj, G.; Masters, D.; Mannucci, A.J. Demonstrating soil moisture remote sensing with observations from the UK TechDemoSat-1 satellite mission. *Geophysical Research Letters* **2016**, *43*, 2016GL068189.
31. Camps, A.; Park, H.; Foti, G.; Gommenginger, C. Ionospheric Effects in GNSS-Reflectometry From Space. *IEEE Journal of Selected Topics in Applied Earth Observations and Remote Sensing* **2016**, *9*, 5851–5861.
32. Elachi, C. *Spaceborne radar remote sensing: Applications and techniques*; IEEE Press: New York, 1988.
33. Hajj, G.A.; Zuffada, C. Theoretical description of a bistatic system for ocean altimetry using the GPS signal. *Radio Science* **2003**, *38*, 1089.
34. Rius, A.; Cardellach, E.; Martin-Neira, M. Altimetric Analysis of the Sea-Surface GPS-Reflected Signals. *IEEE Transactions on Geoscience and Remote Sensing* **2010**, *48*, 2119–2127.
35. Zavorotny, V.U.; Voronovich, A.G. Scattering of GPS signals from the ocean with wind remote sensing application. *IEEE Transactions on Geoscience and Remote Sensing* **2000**, *38*, 951–964.
36. Ridley, J.K.; Partington, K.C. A model of satellite radar altimeter return from ice sheets. *International Journal of Remote Sensing* **1988**, *9*, 601–624.
37. Egbert, G.D.; Erofeeva, S.Y. Efficient Inverse Modeling of Barotropic Ocean Tides. *Journal of Atmospheric and Oceanic Technology* **2002**, *19*, 183–204.
38. Misra, P.; Enge, P. *Global Positioning System: Signals, Measurements and Performance Second Edition*; Ganga-Jamuna Press, 2006.
39. Hernández Pajares, M.; Roma Dollase, D.; Krankowski, A.; García Rigo, A.; Orús Pérez, R. Comparing performances of seven different global VTEC ionospheric models in the IGS context. International GNSS Service Workshop (IGS 2016). International GNSS Service (IGS), 2016, pp. 1–13.

40. Gleason, S.; Hodgart, S.; Sun, Y.; Gommenginger, C.; Mackin, S.; Adjrad, M.; Unwin, M. Detection and Processing of bistatically reflected GPS signals from low Earth orbit for the purpose of ocean remote sensing. *IEEE Transactions on Geoscience and Remote Sensing* **2005**, *43*, 1229–1241.
41. Bracewell, R. *The fourier transform and its application - Cerca amb Google*; Electrical and electronic engineering, McGraw-Hill, 1965.
42. Fujita, S.; Hirabayashi, M.; Goto-Azuma, K.; Dallmayr, R.; Satow, K.; Zheng, J.; Dahl-Jensen, D. Densification of layered firn of the ice sheet at NEEM, Greenland. *Journal of Glaciology* **2014**, *60*, 905–921.
43. Ulaby, F.T.; Moore, R.K.; Fung, A.K. *Microwave remote sensing: Active and passive. Volume 2 - Radar remote sensing and surface scattering and emission theory*; Artech House: Norwood, MA, 1982.
44. Rizzoli, P.; Martone, M.; Rott, H.; Moreira, A. Characterization of Snow Facies on the Greenland Ice Sheet Observed by TanDEM-X Interferometric SAR Data. *Remote Sensing* **2017**, *9*, 315.
45. Mote, T.L.; Anderson, M.R. Variations in snowpack melt on the Greenland ice sheet based on passive-microwave measurements. *Journal of Glaciology* **1995**, *41*, 51–60.
46. Kuipers Munneke, P.; Ligtenberg, S.R.M.; Noël, B.P.Y.; Howat, I.M.; Box, J.E.; Mosley-Thompson, E.; McConnell, J.R.; Steffen, K.; Harper, J.T.; Das, S.B.; van den Broeke, M.R. Elevation change of the Greenland Ice Sheet due to surface mass balance and firn processes, 1960–2014. *The Cryosphere* **2015**, *9*, 2009–2025.
47. Das, S.B.; Joughin, I.; Behn, M.D.; Howat, I.M.; King, M.A.; Lizarralde, D.; Bhatia, M.P. Fracture Propagation to the Base of the Greenland Ice Sheet During Supraglacial Lake Drainage. *Science* **2008**, *320*, 778–781.